

## SUPPLEMENTAL MATERIAL

### Methods

Apatite (U-Th)/He (AHe) and apatite fission track (AFT) thermochronological systems have partial retention temperature of 40-80 °C (Farley, 2000; Wolf et al., 1998) and annealing temperature of 60-110 °C (Ketcham et al., 2007), respectively. Thus, these two methods would provide constraints on exhumation histories of the upper ~2 to 5-km crust. Both AHe and AFT analyses were conducted in the thermochronology lab at the State Key Laboratory of Earthquake Dynamics, Institute of Geology, China Earthquake Administration. Apatite grains were extracted from samples following standard crushing, heavy liquid and magnetic separation procedures.

**Apatite (U-Th)/He Method** Apatite crystals were carefully hand-picked on the basis of morphology (euhedral), size (usually >70-80 µm), and optical clarity (inclusion-free) using a high-power stereo-zoom microscope. Each grain was loaded into a Pt tube and analyzed for He on an Australian Scientific Instruments Alphachron (U-Th)/He system. He was extracted by heating using a Nd-YAG laser heating (8A current) for 5 min, followed by at least one more extraction to ensure complete degassing. The extracted <sup>4</sup>He was spiked with <sup>3</sup>He and measured on a quadrupole mass spectrometer. Then, the degassed grains were dissolved in HNO<sub>3</sub> and the U and Th contents were measured on an Agilent 7900 inductively coupled plasma-mass spectrometry (ICP-MS). Shards of Durango apatite were analyzed with the samples as age standards. Apparent He age of each grain was calculated iteratively based on the equation  $^4\text{He} = 8 \cdot (^{238}\text{U}) \cdot [\exp(\lambda_{238t}) - 1] + 7 \cdot (^{235}\text{U}) \cdot [\exp(\lambda_{235t}) - 1] + 6 \cdot (^{232}\text{Th}) \cdot [\exp(\lambda_{232t}) - 1]$  and corrected for  $\alpha$ -ejection (Ketcham et al., 2011). Mean age was determined using usually 5-7 aliquots for each sample.

**LA-ICP-MS Fission Track Method** Fission-track chronometry is one of the best established low-temperature thermochronometry, which has been widely used to understand exhumation of the shallow crust related to tectonic or climate process (Hurford and Green, 1982; Gleadow et al., 2002). The conventional external detector method (EDM) has been well established to circumvent a serious of uncertainties, including mineral chemistry, absolute value of decay constant, and the efficiency of irradiation (Hasebe et al., 2004). However, due to the environmental and political pressures, the only available reactor in China has been closed to the public and an international delivery was blocked during the coronavirus pandemic. We used laser ablation-inductively coupled plasma mass spectrometry (LA-ICP-MS) method for uranium measurement for FT analysis. To assess the reliability of the LA-ICP-MS fission track method in our laboratory, Pang et al. (2017) analyzed 54 Durango apatite fragments and 38 Fish Canyon Tuff (FCT) apatite fragments. The central ages range from  $31.1 \pm 1.2$  Ma to  $34.1 \pm 1.2$  Ma for Durango apatites, and from  $26.0 \pm 1.0$  Ma to  $29.3 \pm 2.0$  Ma for FCT apatites, which are well consistent with published ages (Mcdowell et al., 2005; Gleadow et al., 2015). The apatite fission-track ages from both the Quyang and Xingtai transects vary systematically with elevation, lending confidence of the reliability of our dating results. Apatite grains were mounted on epoxy slides with araldite epoxy, then etched in 5.5 M HNO<sub>3</sub> at 21 °C for 20 s. U content was determined using a Resolution M50 ArF excimer laser at a wavelength of 193 nm and an Agilent 7900 ICP-MS. A 22 µm square beam was used for all analyses. All the samples passed the chi-

square test. The detailed analytical procedures for sample preparing and analysis using LA-ICP-MS fission-track method can be found in [Pang et al. \(2017\)](#).

**Inverse Thermal History Modeling** To further investigate the thermal evolution of samples from the three transects, thermal history modeling was performed using QTQt (v5.4.0) software based on the Bayesian transdimensional Markov chain Monte Carlo (MCMC) inversion scheme ([Gallagher, 2012](#)). The samples from each transect were treated as a vertical profile. Input data for inversions included AFT and AHe ages, AFT track-length distribution,  $D_{par}$  value, and grain size data. Annealing algorithm for apatite fission track ([Ketcham et al., 2007](#)) and no radiation damage models for apatite helium diffusion ([Farley, 2000](#)) were used for thermal history modeling. Thermal history covers a broad time range from the late Mesozoic to the present and a temperature range over the sensitive regions of the apatite fission-track thermochronometer. Assuming that the paleogeothermal gradient is similar to the present value ( $25 \pm 15$  °C/km), a broad reasonable temperature offset between the uppermost and lowermost was applied to the modeling protocol with sufficient search freedom. The present surface temperature of  $15 \pm 15$  °C was applied for all samples. No other constraints were imposed during the modeling. More than 250,000 iterations for both burn-in and post-burn-in process were used to calculate the average model. AHe ages calculations were tested using no radiation damage and two radiation damage models ([Flowers et al., 2009](#); [Gautheron et al., 2009](#)). No significant differences were observed among these three models.

The agreement between the observed and predicted values is important for assessing the reliability of the inverse thermal histories. Generally, the observed and predicted values of the AHe ages are well consistent for most of the samples from the three transects ([Figures S7, S8, and S9](#)). For the Taibai transect, the expected thermal histories inferred with Flowers' radiation damage model ([Flowers et al., 2009](#)) result in two pulsed rapid cooling. The predictions are in accordance with the observations ([Figure S7](#)). The first rapid cooling occurred at ~50 Ma and the second one occurred at ~25 Ma. The inferred thermal history is consistent with the direct interpretations on the age-elevation relationship, which indicates relatively slow cooling prior to the Oligocene and a phase of rapid cooling commenced at  $26.8 \pm 1.5$  Ma followed by slow cooling. For the Quyang transect, the expected thermal histories indicate two phases of rapid cooling. One occurred at ~50-40 Ma and the other at ~22 Ma. The second phase of cooling is more significant. The AHe ages and apatite fission-track lengths can be reasonably well predicted, while few fission-track ages (QY19-6 and QY19-4) are slightly older than the predicted values. The expected thermal histories of the Xingtai transect is similar to that of the Quyang transect and also show two phases of rapid cooling. The first phase of rapid cooling occurred at ~50-40 Ma following a period of slow cooling since the late Mesozoic. The second phase of rapid cooling occurred at ~28-22 Ma. The AHe ages and fission-track lengths are overall well predicted, but the fission-track ages, particularly for the lower six samples are slightly younger than the predicted values.

### **Additional Interpretation of Anomalously Old AHe Data from the Xingtai Transect**

Apatite (U-Th)/He dating method with low closure temperature (~70 °C) has been applied into a wide range of topics ([Reiners and Brandon, 2006](#)). A key issue in applying this

thermochronometer is the uncertainty and reproducibility in dating results (Green et al., 2006; Gautheron et al., 2009; Reiners et al., 2017). It is quite common that the ages of (U-Th)/He aliquots from the same rock sample spread over a wide range. Many factors are reported to be responsible for the uncertainty and non-reproducibility, such as laboratory procedure, effective uranium (eU) distribution, grain size, and radiation damage (Reiners et al., 2017). However, even considering these factors, the dispersion of (U-Th)/He dating results is large and difficult to understand. In some cases, the (U-Th)/He ages are even significantly older than the fission-track ages from the same sample (Hendriks and Redfield, 2005; Green et al., 2006).

For the Xingtai transect, the distribution of AHe ages shows a correlation with lithology (Figure S6). The ages of the upper three samples (XT19-1, XT19-2, and XT19-3) collected from sandstone generally vary with elevation. Sample XT19-3 has nine aliquots with AHe ages that are generally concentrated, ranging from  $23.0 \pm 0.4$  Ma to  $29.0 \pm 1.1$  Ma. Consistently, the lowest sample XT19-12 collected from granodiorite has five aliquots with AHe ages ranging from  $21.2 \pm 0.8$  Ma to  $33.7 \pm 0.7$  Ma and a mean value of  $26.6 \pm 4.9$  Ma. In contrast, the intermediate six samples (from XT19-5 to XT19-10) are collected from the Archean gneiss, which have AHe ages distributed over a wide range from  $25.6 \pm 0.9$  Ma to  $63.8 \pm 1.3$  Ma. Particularly, most of the AHe ages of the (U-Th)/He aliquots are much older than the fission-track ages from the same sample. If we excluded the AHe ages older than the fission-track ages from the same sample, the AHe ages of two grains from the Archean gneiss are consistent with that from sample XT19-3 at the higher elevation and sample XT19-12 at the lower. There is no correlation between the eU concentration and the AHe age (Figure S4), indicating that radiation damage may be not a major factor responsible for the anomalously older AHe ages. No age-size correlation was seen for each sample from the Xingtai transect, whereas the grain radius of the apatites from the Archean gneiss is generally larger than that of the apatites from the sandstone and granodiorite (Figure S5). The apatites with larger grain size will experience lower fractional losses than smaller ones and will yield older AHe ages. Moreover, the apatites with larger grain size are more likely to contain inclusions, particularly for these collected from metamorphic rocks. Apatite grains from the sandstone sample XT19-3 at the higher elevation and granodiorite sample XT19-12 at the lower elevation have high quality and concentrated AHe ages, lending confidence of the dating results. Meanwhile the AHe ages from these two samples are consistent with that from the two youngest grains collected from the gneiss. Therefore, we tentatively excluded the anomalously older AHe ages that collected from the Archean metamorphic gneiss.

## References

- Chang, J., Qiu, N., Liu, S., Xu, Q., and Liu, N., 2019, Post-Triassic multiple exhumation of the Taihang Mountains revealed via low-T thermochronology: implications for the paleo-geomorphologic reconstruction of the North China Craton: *Gondwana Research*, v. 68, p. 34-49, <https://doi.org/10.1016/j.gr.2018.11.007>.
- Farley, K.A., 2000, Helium diffusion from apatite: General behavior as illustrated by Durango fluorapatite: *Journal of Geophysical Research: Solid Earth*, v. 105, p. 2903-2914, <https://doi.org/10.1029/1999JB900348>.
- Flowers, R.M., Ketcham, R.A., Shuster, D.L., and Farley, K.A., 2009, Apatite (U-Th)/He thermochronometry using a radiation damage accumulation and annealing model: *Geochimica et Cosmochimica acta*, v. 73, p. 2347-2365, <https://doi.org/10.1016/j.gca.2009.01.015>.
- Gallagher, K., 2012, Transdimensional inverse thermal history modeling for quantitative thermochronology: *Journal of Geophysical Research: Solid Earth*, v. 117, <https://doi.org/10.1029/2011JB008825>.

- Gautheron, C., Tassan-Got, L., Barbarand, J., and Pagel, M., 2009, Effect of alpha-damage annealing on apatite (U–Th)/He thermochronology: *Chemical Geology*, v. 266, p. 157-170, <https://doi.org/10.1016/j.chemgeo.2009.06.001>.
- Gleadow, A.J., Belton, D.X., Kohn, B.P., and Brown, R.W., 2002, Fission track dating of phosphate minerals and the thermochronology of apatite: *Reviews in mineralogy and geochemistry*, v. 48, p. 579-630, <https://doi.org/10.2138/rmg.2002.48.16>.
- Gleadow, A., Harrison, M., Kohn, B., Lugo-Zazueta, R., and Phillips, D., 2015, The Fish Canyon Tuff: A new look at an old low-temperature thermochronology standard: *Earth and Planetary Science Letters*, v. 424, p. 95-108, <https://doi.org/10.1016/j.epsl.2015.05.003>.
- Green, P.F., Crowhurst, P.V., Duddy, I.R., Japsen, P., and Holford, S.P., 2006, Conflicting (U–Th)/He and fission track ages in apatite: enhanced He retention, not anomalous annealing behaviour: *Earth and Planetary Science Letters*, v. 250, p. 407-427, <https://doi.org/10.1016/j.epsl.2006.08.022>.
- Hasebe, N., Barbarand, J., Jarvis, K., Carter, A., and Hurford, A.J., 2004, Apatite fission-track chronometry using laser ablation ICP-MS: *Chemical Geology*, v. 207, p. 135-145, <https://doi.org/10.1016/j.chemgeo.2004.01.007>.
- Hendriks, B., and Redfield, T., 2005, Apatite fission track and (U–Th)/He data from Fennoscandia: An example of underestimation of fission track annealing in apatite: *Earth and Planetary Science Letters*, v. 236, p. 443-458, <https://doi.org/10.1016/j.epsl.2005.05.027>.
- Hurford, A.J., and Green, P.F., 1982, A users' guide to fission track dating calibration: *Earth and Planetary Science Letters*, v. 59, p. 343-354, [https://doi.org/10.1016/0012-821X\(82\)90136-4](https://doi.org/10.1016/0012-821X(82)90136-4).
- Ketcham, R.A., Carter, A., Donelick, R.A., Barbarand, J., and Hurford, A.J., 2007, Improved modeling of fission-track annealing in apatite: *American Mineralogist*, v. 92, p. 799-810, <https://doi.org/10.2138/am.2007.2281>.
- Ketcham, R.A., Gautheron, C., and Tassan-Got, L., 2011, Accounting for long alpha-particle stopping distances in (U–Th–Sm)/He geochronology: Refinement of the baseline case: *Geochimica et Cosmochimica Acta*, v. 75, p. 7779-7791, <https://doi.org/10.1016/j.gca.2011.10.011>.
- Li, Y., Zhang, W., Yuan, B., Han, W., Chen, G., and Zhang, L., 2018, Basement composition for Weihe Cenozoic Basin and its petroleum geological significance: *Journal of Xi'an University of Science and Technology*, v. 38, p. 966-974, <https://doi.org/10.13800/j.cnki.xakjdxxb.2018.0613>.
- McDowell, F.W., McIntosh, W.C., and Farley, K.A., 2005, A precise  $^{40}\text{Ar}$ – $^{39}\text{Ar}$  reference age for the Durango apatite (U–Th)/He and fission-track dating standard: *Chemical Geology*, v. 214, p. 249-263, <https://doi.org/10.1016/j.chemgeo.2004.10.002>.
- Pang, J., Zheng, D., Ma, Y., Wang, Y., Wu, Y., Wan, J., Yu, J., Li, Y., and Wang, Y., 2017, Combined apatite fission-track dating, chlorine and REE content analysis by LA-ICPMS: *Science Bulletin*, v. 62, p. 1497-1500, <https://doi.org/10.1016/j.scib.2017.10.009>.
- Qing, J., Ji, J., Wang, J., Peng, Q., Niu, X., and Ge, Z., 2008, Apatite fission track study of Cenozoic uplifting and exhumation of Wutai Mountain, China: *Chinese Journal of Geophysics*, v. 51, p. 256-264, <https://doi.org/10.1002/cjg2.1217>.
- Reiners, P.W., and Brandon, M.T., 2006, Using thermochronology to understand orogenic erosion: *Annual Review of Earth and Planetary Sciences*, v. 34, p. 419-466, <https://doi.org/10.1146/annurev.earth.34.031405.125202>.
- Reiners, P.W. et al. *Geochronology and thermochronology*. John Wiley & Sons, 2017.
- Wolf, R., Farley, K., and Kass, D., 1998, Modeling of the temperature sensitivity of the apatite (U–Th)/He thermochronometer: *Chemical Geology*, v. 148, p. 105-114, [https://doi.org/10.1016/S0009-2541\(98\)00024-2](https://doi.org/10.1016/S0009-2541(98)00024-2).



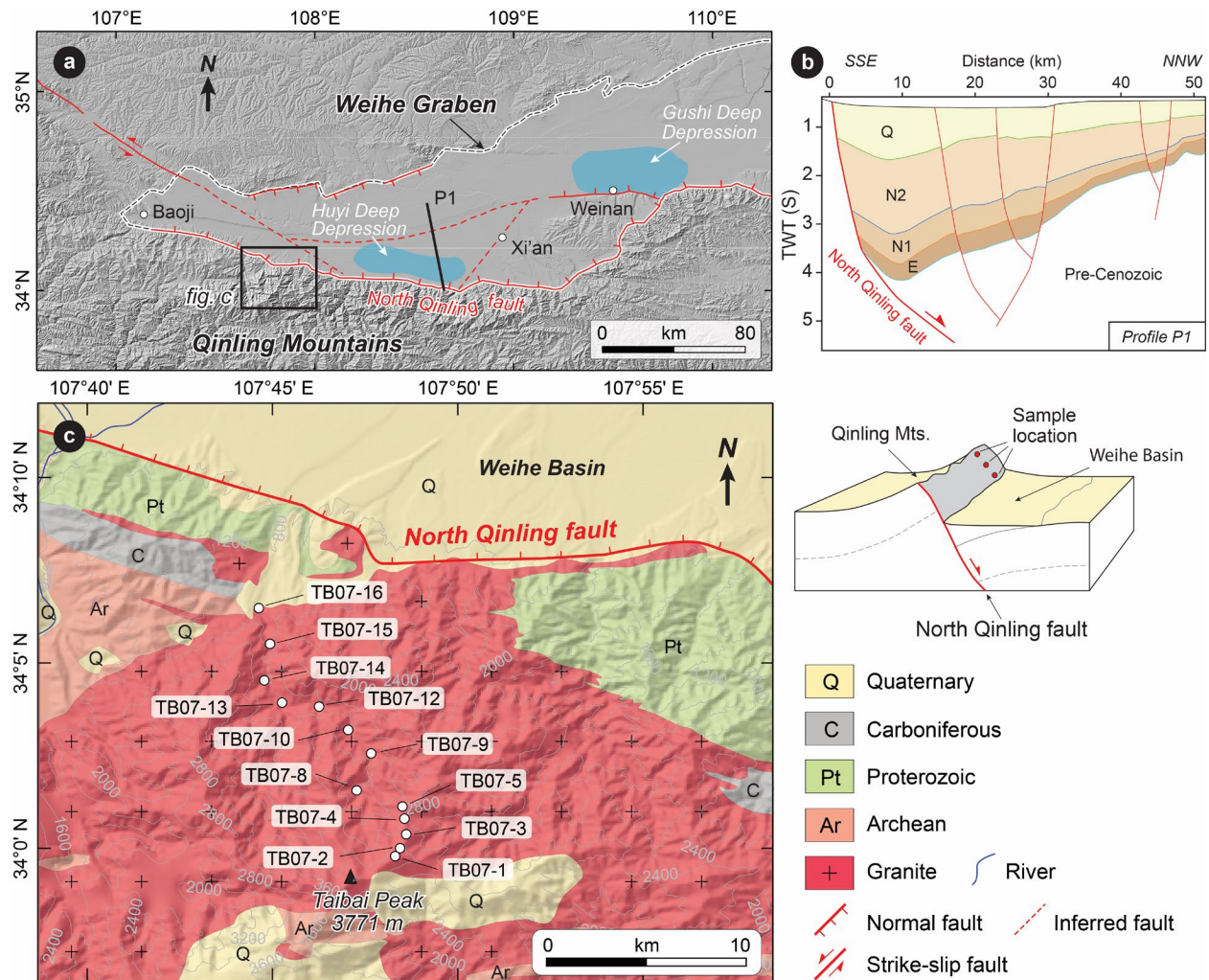


**Figure S1** (a) Shaded relief map of the Weihe Graben. Black dashed line refers to the area of the Weihe Graben. Red lines indicate the locations of faults. The location of a NNW-SSE-trending geophysical survey profile (P1) is shown. (b) A seismic reflection profile shows half-graben deposition in the Weihe Graben (Li et al., 2018), which is largely controlled by the North Qinling fault. The Cenozoic deposition began at the Eocene and accelerated at the early Neogene. (c) Geologic map of the northern Qinling showing sample locations of the Taibai transect. See the location in Fig. a. A schematic model on the right side shows the sampling locations in the uplifted footwall of a normal fault.

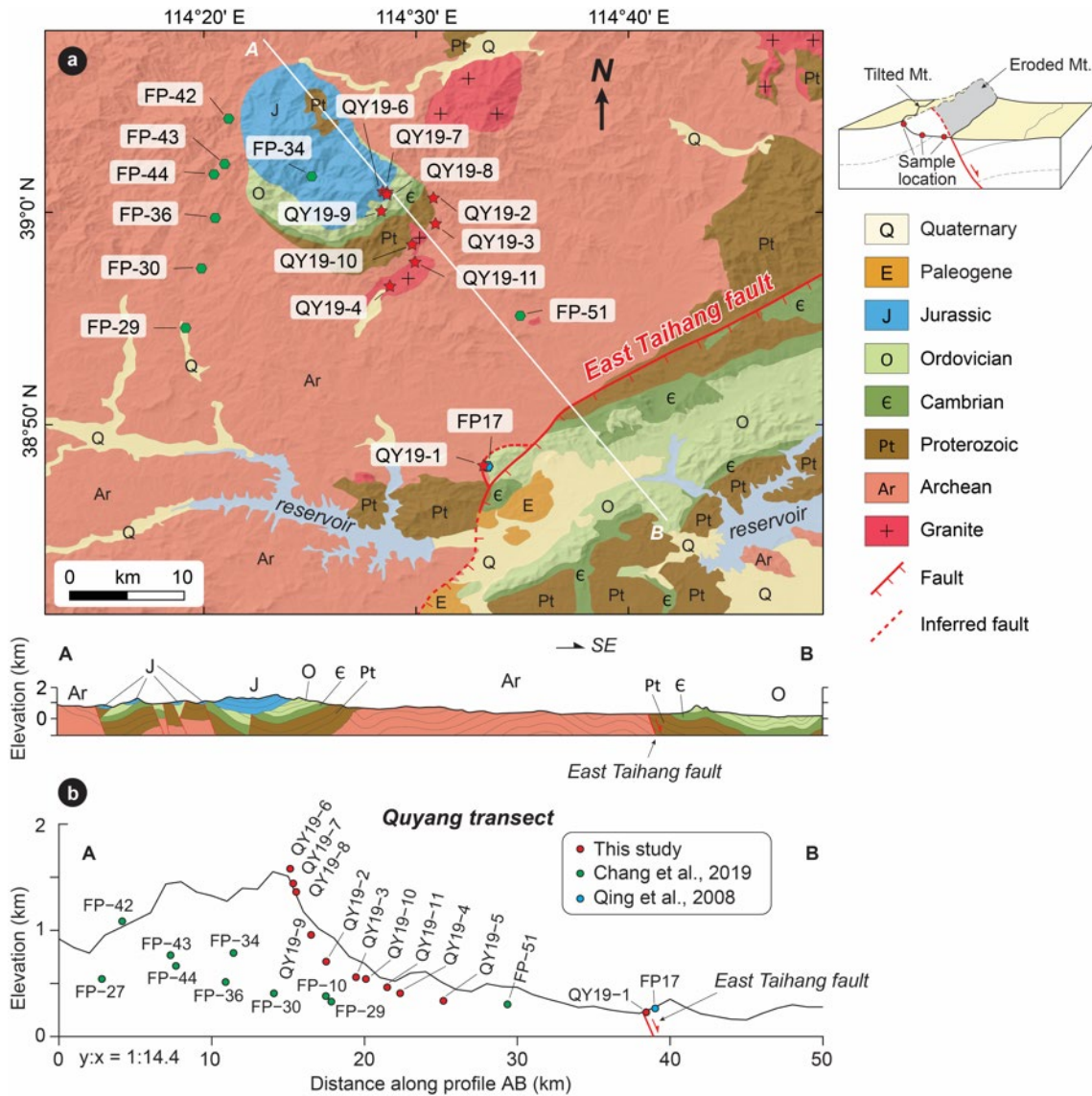


**Figure S2** (a) Geologic map show sample locations of the Quyang transect in this study (red star), Chang et al. (2019) (green hexagon), and Qing et al. (2008) (blue hexagon). See location in Figure 1. A NW-SE-trending geologic profile (A-B) was extracted based on the geologic map. A schematic model on the right side shows the sampling locations in the uplifted footwall of the normal East Taihang fault. (b) A topographic profile along A-B show the sampling locations.

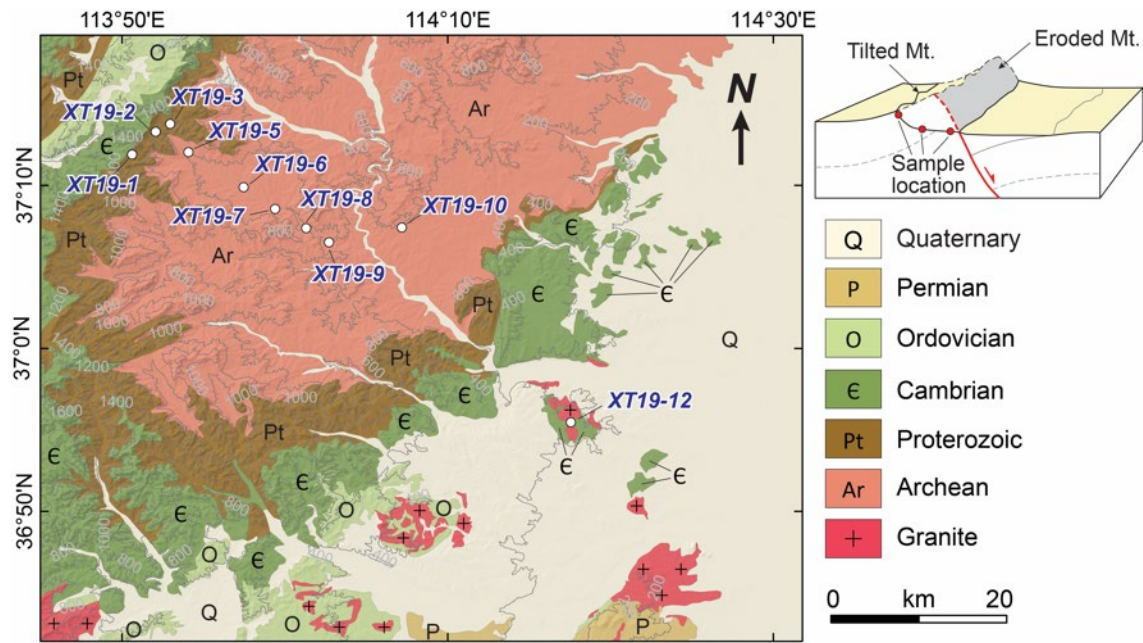


**Figure S3** Geologic map show sample locations of the Xingtai transect in this study. See location in Figure 1. A schematic model on the right side shows the sampling locations in the uplifted footwall of the normal East Taihang fault. The exact location of the East Taihang fault was not identified due to the covering Quaternary deposition.



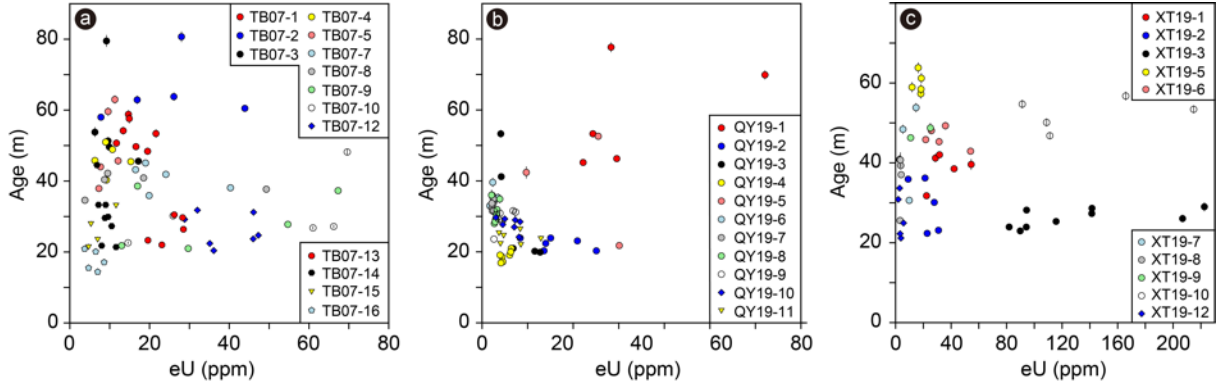


**Figure S4** Relationship between apatite (U-Th)/He age and eU concentration in multigrain aliquots of the samples from the Taibai (a), Quyang (b), and Xingtai (c) transects.

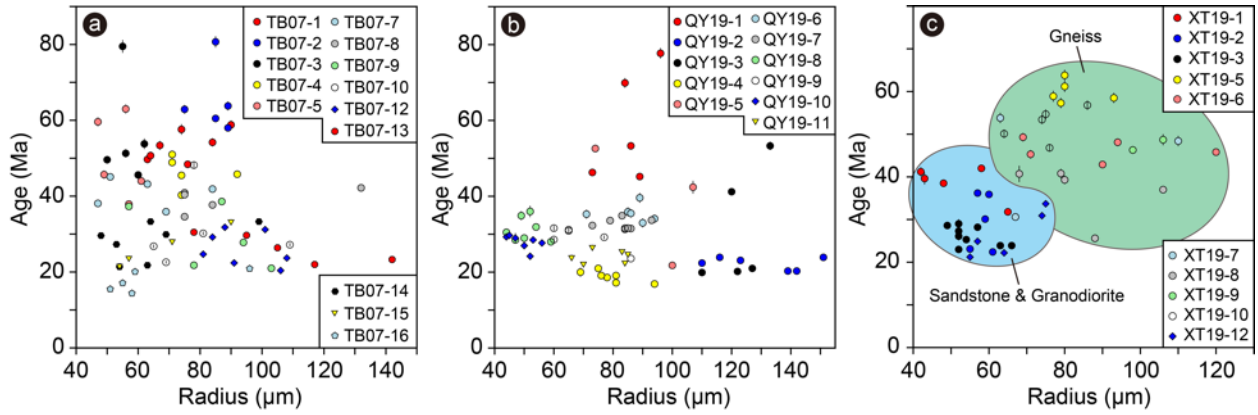


**Figure S5** Relationship between apatite (U-Th)/He age and grain radius in multigrain aliquots of samples from the Taibai (a), Quyang (b), and Xingtai (c) transects.



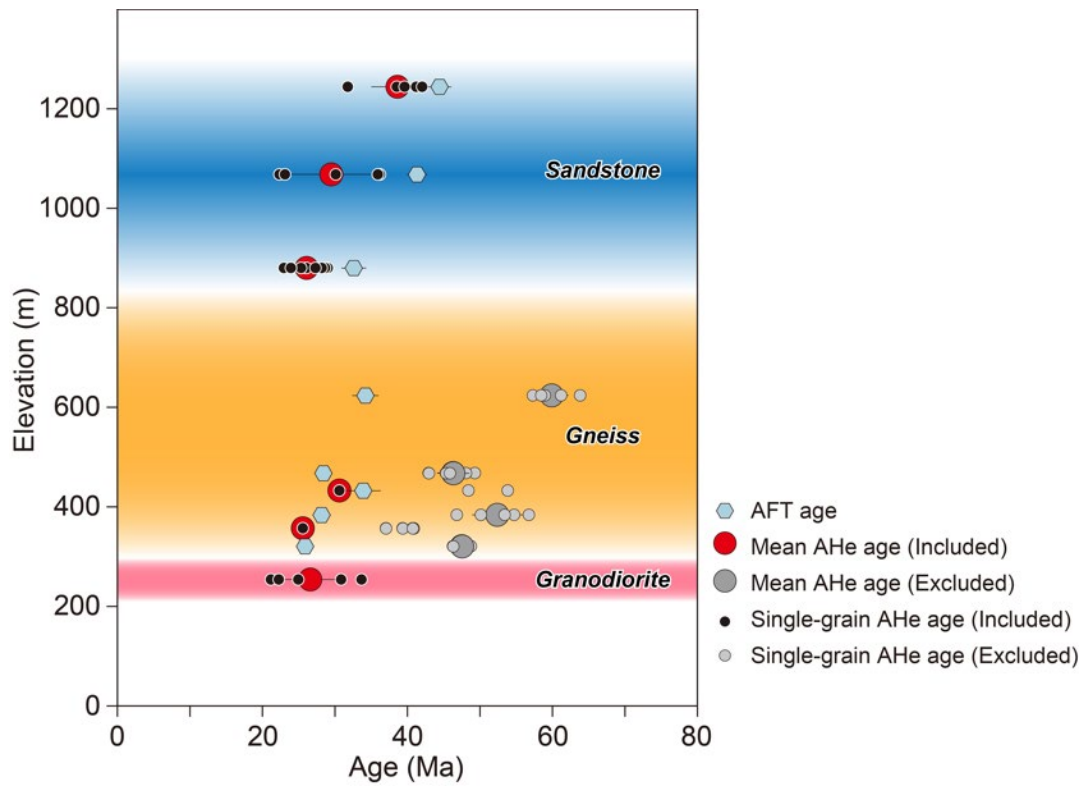


**Figure S6** Age-elevation relationship of samples from the Xingtai transect. All the anomalously older AHe ages, which are older than the fission-track ages from the same sample, are from the samples collected from the Archean gneiss.

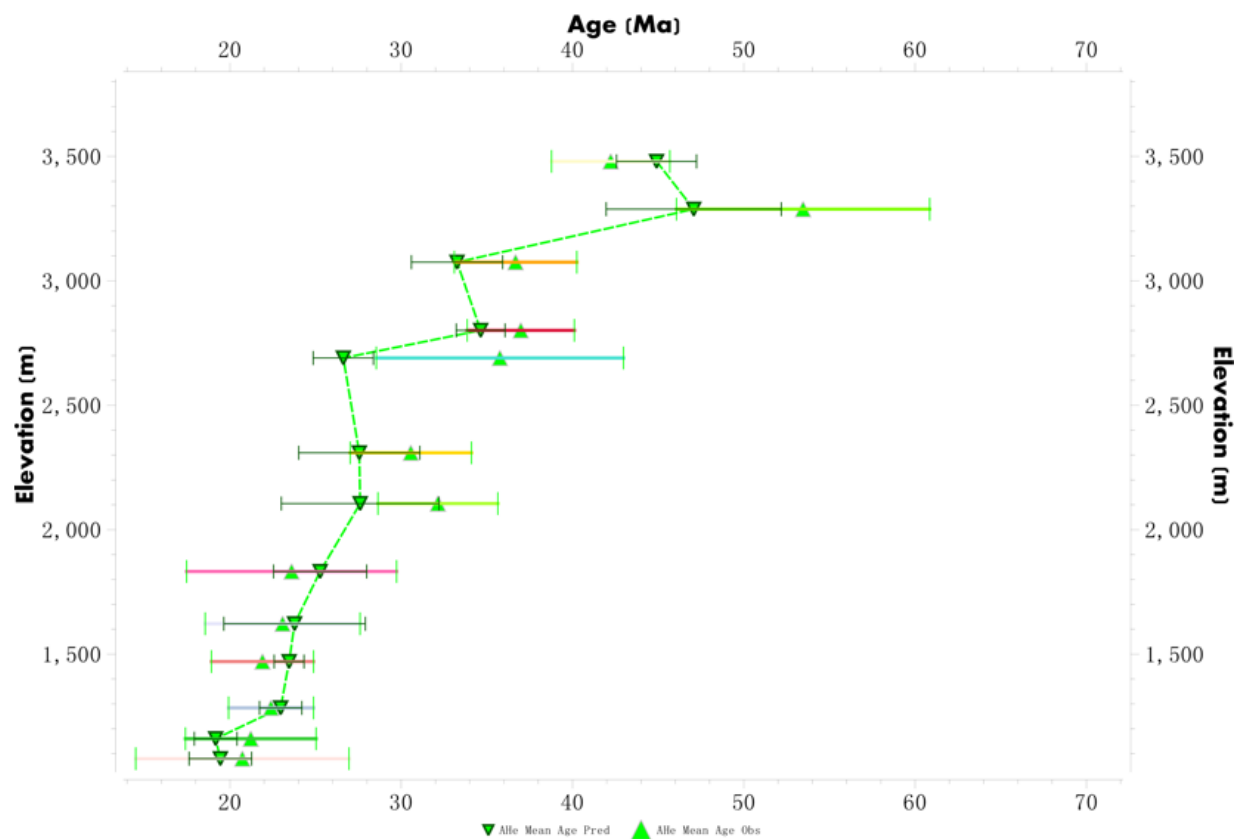


**Figure S7** Age-elevation relationship from the Taibai transect comparing the AHe observations with predictions derived from the expected thermal histories in QTQt. The mean for the observed AHe ages are shown as upward triangles, and the mean of the predictions as downward triangles.

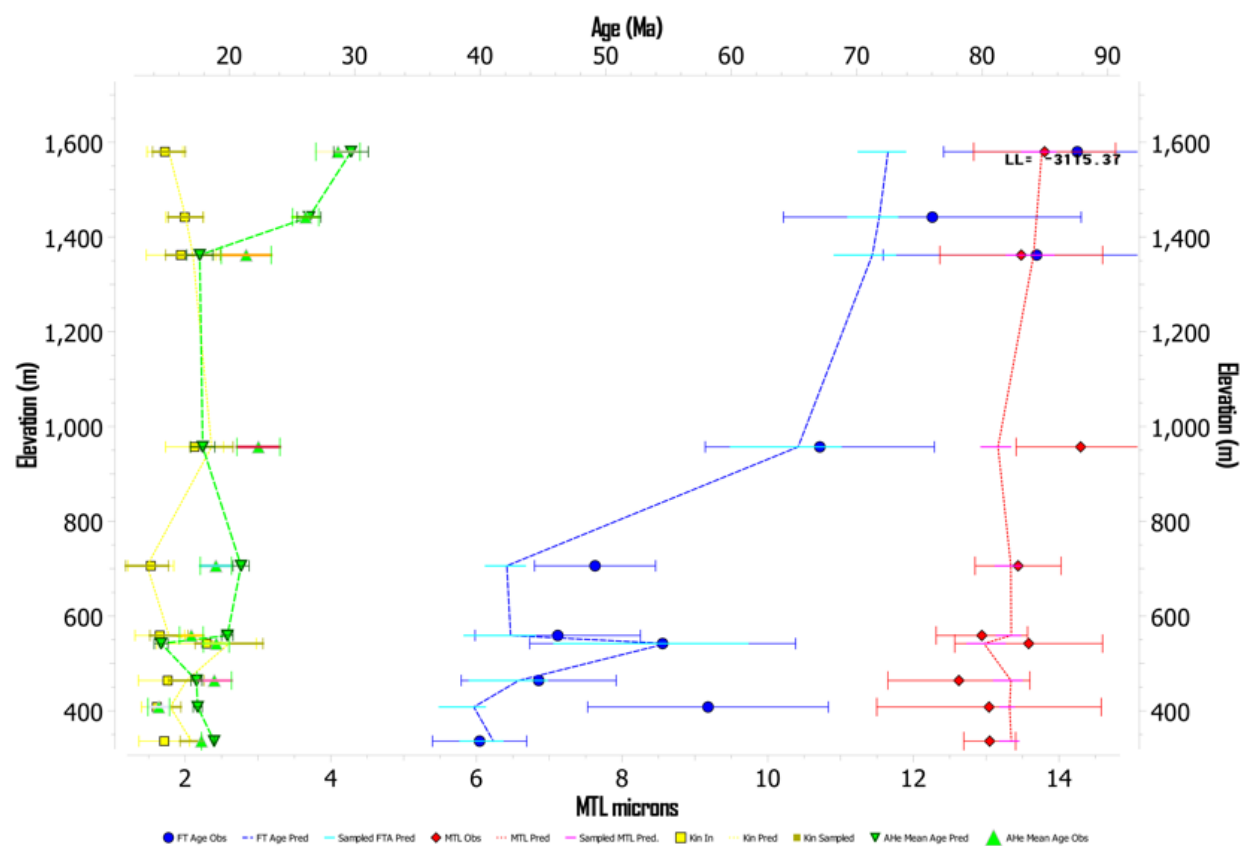


**Figure S8** Age-elevation and length-elevation relationships from the Quyang transect comparing the observations of the AFT and AHe ages and the AFT lengths with predictions derived from expected thermal histories in QTQt.

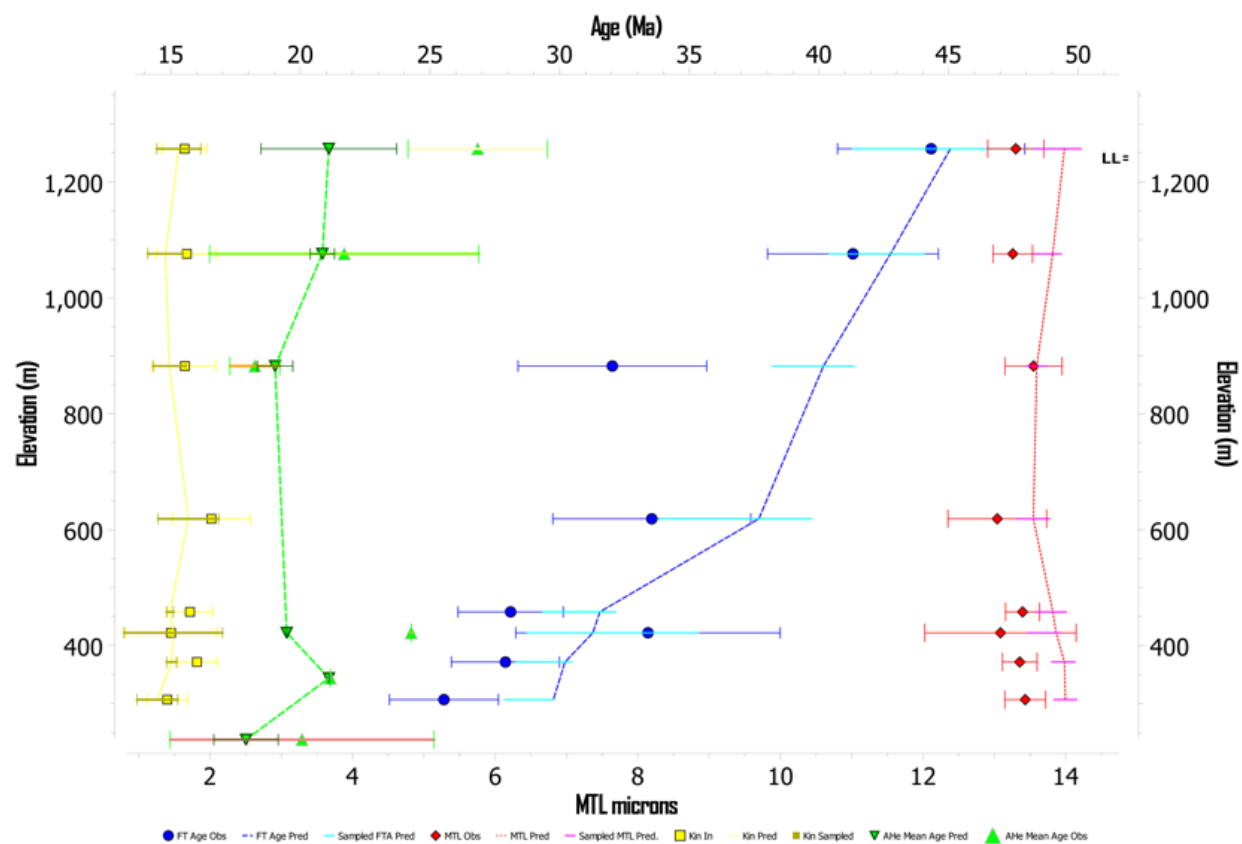


**Figure S9** Age-elevation and length-elevation relationships from the Xingtai transect comparing the observations of the AFT and AHe ages and the AFT lengths with predictions derived from expected thermal histories in QTQt.



**Table S1 Sample location and lithology**

<b>Sample ID</b>	<b>Longitude (°E)</b>	<b>Latitude (°N)</b>	<b>Elevation (m)</b>	<b>Lithology</b>
<b><i>Taibai transect</i></b>				
TB07-1	107.8052	33.9964	3480	Granite
TB07-2	107.8074	34.0000	3288	Granite
TB07-3	107.8102	34.0062	3075	Granite
TB07-4	107.8094	34.0133	2801	Granite
TB07-5	107.8085	34.0187	2690	Granite
TB07-7	107.7993	34.0167	2309	Granite
TB07-8	107.7879	34.0259	2105	Granite
TB07-9	107.7945	34.0426	1832	Granite
TB07-10	107.7841	34.0532	1622	Granite
TB07-12	107.7710	34.0636	1470	Granite
TB07-13	107.7543	34.0654	1284	Granite
TB07-14	107.7464	34.0754	1160	Granite
TB07-15	107.7489	34.0918	1080	Granite
TB07-16	107.7439	34.1079	990	Granite
<b><i>Quyang transect</i></b>				
QY19-1	114.5437	38.8027	229	Gneiss
QY19-2	114.5136	39.0122	706	Gneiss
QY19-3	114.5152	38.9921	559	Gneiss
QY19-4	114.4794	38.9430	408	Granite
QY19-5	114.4435	38.8944	336	Gneiss
QY19-6	114.4739	39.0174	1580	Breccia
QY19-7	114.4772	39.0170	1442	Breccia
QY19-8	114.4771	39.0147	1362	Breccia
QY19-9	114.4727	39.0021	957	Gneiss
QY19-10	114.4968	38.9758	542	Granite
QY19-11	114.4990	38.9619	464	Granite
<b><i>Xingtai transect</i></b>				
XT19-1	113.8436	37.1981	1244	Sandstone
XT19-2	113.8678	37.2215	1068	Sandstone
XT19-3	113.8827	37.2294	880	Sandstone
XT19-5	113.9014	37.2006	624	Gneiss
XT19-6	113.9578	37.1648	468	Gneiss
XT19-7	113.9883	37.1434	433	Gneiss
XT19-8	114.0219	37.1228	357	Gneiss
XT19-9	114.0452	37.1083	321	Gneiss
XT19-10	114.1198	37.1234	384	Gneiss
XT19-12	114.2929	36.9243	254	Granodiorite

Table S2 Apatite (U-Th)/He data of the Taibai, Quyang, and Xingtai transects

Sample	U (ppm)	Th (ppm)	He (nmol/g)	eU (ppm)	Mass ( $\mu$ g)	Length ( $\mu$ m)	Radius ( $\mu$ m)	Ft <sup>*</sup>	Raw age (Ma)	err (1 $\sigma$ )	Corr age (Ma)	err (1 $\sigma$ )
<i>Taibai transect</i>												
TB07-1-1	11.3	9.3	3.2	13.4	14.1	288	84	0.82	44.4	0.9	54.2	1.1
TB07-1-2	12.7	8.5	3.9	14.7	16.1	268	90	0.83	48.9	1	58.8	1.2
TB07-1-3	13.1	8	3.7	14.9	9.3	242	74	0.79	45.8	1.1	57.6	1.4
TB07-1-4	17.2	10	4.1	19.5	9.4	207	76	0.8	38.8	0.8	48.4	1.0
TB07-1-5	14.2	10.1	3.4	16.6	5.4	176	63	0.76	37.8	0.8	49.7	1.0
TB07-1-6	19	11.3	4.8	21.6	6.5	187	67	0.77	41.3	0.9	53.4	1.2
TB07-1-7	10.3	5.8	2.4	11.7	5.6	183	64	0.76	38.6	0.8	50.7	1.1
<b>TB07-1</b>											<b>53.3</b>	<b>3.7<sup>##</sup></b>
TB07-2-1**	27.4	2.2	10.0	28	13.4	252	85	0.82	66.3	1.2	80.7	1.5
TB07-2-2	25.6	1.8	7.5	26.1	15.4	256	89	0.83	53	1	63.8	1.2
TB07-2-3	15.6	4.6	4.5	16.9	9.5	236	75	0.8	50.1	1	62.9	1.2
TB07-2-4	42.9	3.8	11.8	43.9	13.2	229	85	0.82	49.8	0.9	60.5	1.0
TB07-2-5	5.5	9.6	2.0	7.8	14.7	228	89	0.83	48.1	0.8	58.0	0.9
<b>TB07-2</b>											<b>61.3</b>	<b>2.3</b>
TB07-3-1	7.4	7.8	1.9	9.6	4.3	199	56	0.73	37.5	0.8	51.3	1.1
TB07-3-2	5	4.7	1.3	6.3	5.5	195	62	0.76	40.7	1.1	53.8	1.4
TB07-3-3	13.9	13	3.1	17.2	4.9	194	60	0.75	34	0.6	45.6	0.9
TB07-3-4	7.9	6.4	1.7	9.9	2.9	170	50	0.69	34.5	0.7	49.6	1.0
TB07-3-5**	6.9	7.9	2.7	9.2	4.2	213	55	0.72	57.6	1.3	79.5	1.7
<b>TB07-3</b>											<b>50.1</b>	<b>3.0</b>
TB07-4-1	5.6	2.7	1.3	6.3	17.1	262	92	0.84	38.2	0.8	45.8	0.9
TB07-4-2	8	3.7	1.9	9	9.2	279	71	0.79	40.1	0.8	51.0	1.0
TB07-4-3	13.7	5.9	2.9	15.3	8.1	163	74	0.79	36.1	0.7	45.5	0.9
TB07-4-4	9.7	3.4	2.2	10.7	7.6	183	71	0.79	38.5	0.8	48.9	1.0
TB07-4-5	8.1	3.6	1.6	9.2	9.1	230	74	0.79	32	0.7	40.3	0.8
<b>TB07-4</b>											<b>46.3</b>	<b>3.6</b>
TB07-5-1	4.4	13	1.3	7.7	4.9	166	61	0.75	33	0.7	44.0	0.9

TB07-5-2	7.2	16.2	2.7	11.3	3.9	176	56	0.73	45.8	0.9	63.0	1.2
TB07-5-3	4.3	11.2	1.1	7.3	4.2	172	57	0.74	27.9	0.5	37.9	0.7
TB07-5-4	7.7	16.4	2.0	12.1	2.7	157	49	0.69	31.7	0.7	45.7	1.1
TB07-5-5	5.1	16.6	2.0	9.6	2.5	170	47	0.68	40.4	0.8	59.6	1.2
<b>TB07-5</b>											<b>50.0</b>	<b>9.6</b>
TB07-7-1	17.8	8.9	3.0	19.9	7.1	201	69	0.78	27.9	0.5	35.9	0.6
TB07-7-2	14.5	8.7	2.9	16.5	5.3	168	63	0.76	32.8	0.6	43.2	0.8
TB07-7-3	35.7	20.0	5.5	40.3	2.3	138	47	0.68	25.9	0.6	38.1	0.9
TB07-7-4	21.1	13.1	4.5	24.1	14.6	308	84	0.82	34.4	0.6	41.9	0.7
TB07-7-5	16.8	9.3	3.2	19.0	3.1	172	51	0.70	31.8	0.6	45.1	0.8
<b>TB07-7</b>											<b>40.8</b>	<b>3.4</b>
TB07-8-1	40.8	36.4	8.2	49.3	12.6	235	84	0.82	30.9	0.5	37.7	0.6
TB07-8-2	3	2.9	0.5	3.8	9.2	217	75	0.8	27.6	0.8	34.6	0.9
TB07-8-3	15.4	12.6	3.2	18.5	9.1	214	75	0.8	32.6	0.6	40.9	0.8
TB07-8-4	7	6.6	1.5	8.7	9.4	220	75	0.8	32.3	0.6	40.4	0.8
TB07-8-5	7.7	7.5	1.9	9.5	48.1	337	132	0.89	37.3	0.7	42.2	0.7
<b>TB07-8</b>											<b>39.2</b>	<b>2.7</b>
TB07-9-1	19.8	42.6	2.9	29.7	25.3	332	103	0.85	17.9	0.3	21.0	0.3
TB07-9-2	10.5	10.9	1.2	13	11.1	259	78	0.81	17.6	0.3	21.8	0.4
TB07-9-3	44.7	43.4	6.9	54.7	18.4	278	94	0.84	23.3	0.4	27.8	0.5
TB07-9-4	53.3	61	10.0	67.3	4.7	228	57	0.73	27.4	0.5	37.3	0.6
TB07-9-5	10.9	26.4	3.0	17	14.9	273	87	0.83	31.8	0.5	38.6	0.6
<b>TB07-9</b>											<b>29.3</b>	<b>7.5</b>
TB07-10-1**	63.7	25.8	14.7	69.6	10.8	241	78	0.81	38.9	0.7	48.2	0.8
TB07-10-2	57.6	37.6	8.4	66.2	27.4	289	109	0.86	23.4	0.4	27.2	0.5
TB07-10-3	55.6	23.6	6.8	61	5.9	181	65	0.77	20.5	0.4	26.8	0.5
TB07-10-4	22.8	13.3	3.4	25.9	10.8	201	81	0.81	24.5	0.4	30.2	0.5
TB07-10-5	13.7	4.1	1.4	14.6	6.7	165	69	0.78	17.6	0.3	22.6	0.4
<b>TB07-10</b>											<b>26.7</b>	<b>2.7</b>
TB07-12-1	29.9	9	4.6	32	15.5	283	88	0.83	26.3	0.5	31.8	0.6
TB07-12-2	43.2	12.2	5.1	46	27.4	300	108	0.86	20.3	0.4	23.7	0.4
TB07-12-3	26.4	10.6	3.7	28.8	12.1	201	84	0.82	23.9	0.5	29.2	0.6

TB07-12-4	42.3	16.5	6.6	46.1	26.1	390	101	0.85	26.5	0.4	31.2	0.5
TB07-12-5	33	13.5	3.4	36.1	28.4	372	106	0.86	17.5	0.3	20.4	0.4
TB07-12-6	42.7	19.9	5.2	47.3	12.7	278	81	0.81	20.1	0.4	24.7	0.5
TB07-12-7	32.7	10.4	3.5	35.1	16.2	254	91	0.83	18.7	0.3	22.4	0.4
<b>TB07-12</b>											<b>26.2</b>	<b>4.2</b>
TB07-13-1	25.9	10.3	3.8	28.3	18.6	264	95	0.84	24.9	0.4	29.7	0.5
TB07-13-2	26.1	10.5	3.5	28.5	25	305	105	0.85	22.6	0.4	26.4	0.5
TB07-13-3	20.9	9.7	2.4	23.1	34.7	330	117	0.87	19.1	0.3	22.0	0.4
TB07-13-4	17.2	10.5	2.2	19.6	61.7	389	142	0.89	20.8	0.3	23.3	0.4
TB07-13-5	24	9.6	3.5	26.2	10.6	236	78	0.81	24.6	0.5	30.5	0.6
<b>TB07-13</b>											<b>26.4</b>	<b>3.4</b>
TB07-14-1	6.8	9.3	1.2	9	5.5	169	64	0.76	25.4	0.5	33.3	0.7
TB07-14-2	8.5	8.7	1.1	10.5	3.5	179	53	0.72	19.5	0.5	27.3	0.7
TB07-14-3	4.6	11.5	1.1	7.2	23.2	341	99	0.85	28.2	0.5	33.3	0.5
TB07-14-4	6	8.5	0.7	8	5.8	202	63	0.76	16.6	0.4	21.8	0.5
TB07-14-5	6.5	10.2	1.0	8.8	2.6	167	48	0.68	20.2	0.5	29.6	0.7
TB07-14-6	6.6	21.7	1.0	11.6	3.4	161	54	0.72	15.3	0.4	21.4	0.5
TB07-14-7	7.3	9.8	1.2	9.6	6.6	165	69	0.78	23.3	0.5	29.9	0.6
<b>TB07-14</b>											<b>28.1</b>	<b>4.5</b>
TB07-15-1	5.2	8	0.7	7	4.3	184	57	0.74	17.5	0.4	23.7	0.6
TB07-15-2	8.7	12.8	1.8	11.6	15.9	268	90	0.83	27.7	0.5	33.3	0.6
TB07-15-3	3.8	6.9	0.6	5.3	7.5	192	71	0.78	22.1	0.5	28.1	0.6
TB07-15-4	3.1	6.8	0.4	4.7	3.4	149	54	0.72	15.6	0.5	21.6	0.7
<b>TB07-15</b>											<b>26.7</b>	<b>4.5</b>
TB07-16-1	4.4	9.3	0.5	6.5	4.5	168	59	0.74	15	0.4	20.1	0.5
TB07-16-2	4.6	10.3	0.4	7	4.4	187	58	0.74	10.6	0.3	14.4	0.4
TB07-16-3	6.1	11.3	0.6	8.6	3.7	169	55	0.72	12.4	0.3	17.1	0.4
TB07-16-4	3.5	5.3	0.3	4.7	3.1	178	51	0.7	10.9	0.4	15.5	0.6
TB07-16-5	2.5	5	0.4	3.7	18.4	251	96	0.84	17.6	0.4	20.9	0.5
<b>TB07-16</b>											<b>17.6</b>	<b>2.5</b>
<b>Quyung transect</b>												
QY19-1-1	28.9	2.6	6.1	29.6	10.0	311	73	0.83	38.2	0.7	46.3	0.9



QY19-1-2	60.6	6.3	19.6	62.1	10.7	277	84	0.84	58.4	1.1	69.9	1.3
QY19-1-3	24.0	1.6	5.9	24.3	13.8	361	86	0.84	44.7	0.8	53.3	1.0
QY19-1-4	21.8	1.7	4.6	22.2	15.0	366	89	0.84	38.1	0.7	45.2	0.8
QY19-1-5	27.6	3.1	10.3	28.3	22.4	400	96	0.87	67.3	1.2	77.7	1.4
<b>QY19-1</b>											<b>58.5</b>	<b>13.0</b>
QY19-2-1	12.0	6.8	1.3	13.6	50.6	457	142	0.90	18.2	0.3	20.3	0.3
QY19-2-2	22.5	11.0	2.5	25.1	66.3	559	139	0.91	18.4	0.3	20.3	0.3
QY19-2-3	5.5	12.1	1.0	8.4	84.6	480	151	0.90	21.5	0.4	23.9	0.4
QY19-2-4	13.4	7.0	1.7	15.1	36.8	339	116	0.87	20.9	0.4	23.9	0.5
QY19-2-5	12.7	5.5	1.5	14.0	32.3	335	110	0.87	19.4	0.4	22.4	0.4
QY19-2-6	17.1	16.4	2.3	20.9	44.8	382	123	0.88	20.3	0.4	23.1	0.4
<b>QY19-2</b>											<b>22.3</b>	<b>1.5</b>
QY19-3-1	11.0	2.5	1.1	11.6	35.9	460	122	0.88	17.9	0.3	20.2	0.3
QY19-3-2**	3.9	1.2	0.8	4.2	39.4	330	120	0.88	36.2	0.7	41.2	0.8
QY19-3-3	12.0	3.1	1.2	12.7	33.1	364	110	0.87	17.2	0.3	19.9	0.4
QY19-3-4**	4.0	0.4	1.1	4.1	53.5	350	133	0.89	47.5	1.0	53.3	1.1
QY19-3-5	6.5	1.2	0.7	6.8	45.9	335	127	0.89	18.6	0.4	21.0	0.5
<b>QY19-3</b>											<b>20.3</b>	<b>0.5</b>
QY19-4-1	4.0	10.3	0.6	6.4	11.7	349	75	0.81	16.9	0.3	21.0	0.3
QY19-4-2	3.7	9.9	0.5	6.1	16.7	385	81	0.84	16.1	0.3	19.1	0.3
QY19-4-3	4.7	6.9	0.5	6.3	7.5	186	69	0.79	15.8	0.3	20.0	1.2
QY19-4-4	2.7	7.0	0.4	4.4	10.7	180	78	0.81	15.1	0.5	18.6	0.6
QY19-4-5	3.1	6.0	0.3	4.5	13.3	272	81	0.82	14.1	0.5	17.2	0.6
QY19-4-6	2.5	7.2	0.3	4.2	22.4	352	94	0.84	14.2	0.5	16.9	0.6
QY19-4-7	2.2	7.3	0.3	3.9	10.8	242	76	0.80	15.4	0.5	19.1	0.6
<b>QY19-4</b>											<b>18.8</b>	<b>1.3</b>
QY19-5-1	27.6	10.8	3.0	30.1	19.5	372	100	0.86	18.7	0.3	21.8	0.4
QY19-5-2**	21.9	15.2	5.9	25.5	8.6	296	74	0.81	42.6	0.8	52.6	1.0
QY19-5-3**	8.8	3.8	1.9	9.7	27.2	260	107	0.86	36.7	1.5	42.4	1.7
<b>QY19-5</b>											<b>21.8</b>	<b>0.4</b>
QY19-6-1	1.7	7.5	0.5	3.5	8.9	232	71	0.79	27.9	0.9	35.3	1.2
QY19-6-2	1.2	4.4	0.4	2.3	14.6	247	85	0.82	29.6	1.0	35.9	1.2

QY19-6-3	1.1	5.3	0.4	2.3	15.9	238	89	0.83	32.8	1.1	39.6	1.3
QY19-6-4	0.8	3.9	0.3	1.7	21.5	381	90	0.83	27.4	1.0	33.0	1.2
QY19-6-5	1.0	5.5	0.4	2.3	15.1	247	86	0.82	29.3	0.9	35.5	1.1
QY19-6-6	1.3	5.4	0.4	2.5	19.2	255	94	0.84	28.6	0.9	34.1	1.1
<b>QY19-6</b>											<b>35.6</b>	<b>2.0</b>
QY19-7-1	1.4	6.3	0.4	2.8	15.6	267	86	0.82	26.0	0.8	31.5	0.0
QY19-7-2	1.3	4.6	0.4	2.4	13.2	290	79	0.81	27.2	0.6	33.6	0.7
QY19-7-3	1.4	5.5	0.4	2.7	17.7	359	84	0.82	25.7	0.5	31.3	0.6
QY19-7-4	1.1	4.4	0.3	2.2	9.7	240	73	0.80	25.7	0.5	32.3	0.7
QY19-7-5	1.3	5.0	0.4	2.5	14.9	290	83	0.82	28.6	0.6	34.9	0.8
QY19-7-6	1.2	4.4	0.3	2.2	15.8	295	85	0.82	26.0	0.6	31.6	0.7
QY19-7-7	1.2	4.0	0.3	2.2	23.0	371	93	0.84	28.2	0.5	33.7	0.6
<b>QY19-7</b>											<b>32.7</b>	<b>1.3</b>
QY19-8-1	1.6	7.4	0.4	3.3	4.4	209	54	0.73	23.2	0.6	31.9	0.9
QY19-8-2	1.7	9.3	0.5	3.9	3.1	175	49	0.70	24.5	0.8	34.9	1.2
QY19-8-3	1.7	6.2	0.3	3.1	2.2	156	44	0.67	20.5	0.7	30.5	1.0
QY19-8-4	1.1	7.9	0.3	2.9	3.3	174	50	0.70	20.4	0.6	29.0	0.9
QY19-8-5	1.1	4.1	0.3	2.1	3.4	161	52	0.72	25.9	1.1	36.0	1.5
QY19-8-6	1.2	6.2	0.3	2.7	4.7	168	59	0.75	21.0	0.5	28.0	0.7
QY19-8-7	1.1	7.6	0.3	2.9	2.5	137	47	0.69	19.7	0.6	28.5	0.9
<b>QY19-8</b>											<b>31.3</b>	<b>2.9</b>
QY19-9-1	3.4	17.0	1.0	7.4	4.8	210	65	0.77	23.9	0.4	31.2	0.5
QY19-9-2	3.1	15.7	0.9	6.8	4.6	242	60	0.75	23.7	0.5	31.6	0.7
QY19-9-3	1.7	8.5	0.5	3.7	12.4	287	77	0.80	23.4	0.4	29.2	0.5
QY19-9-4	1.8	9.0	0.5	3.9	7.6	256	65	0.77	23.7	0.5	30.9	0.7
QY19-9-5	1.2	5.8	0.4	2.6	15.1	290	84	0.82	25.9	0.6	31.6	0.7
QY19-9-6	2.0	10.4	0.5	4.4	6.0	233	60	0.75	21.5	0.4	28.6	0.6
QY19-9-7	1.3	5.8	0.3	2.6	16.2	289	86	0.82	19.5	0.4	23.6	0.0
<b>QY19-9</b>											<b>29.5</b>	<b>2.6</b>
QY19-10-1	3.4	15.8	0.8	7.1	2.7	154	50	0.74	20.1	0.5	27.0	0.7
QY19-10-2	3.8	19.6	1.0	8.3	3.3	183	53	0.75	21.3	0.6	28.5	0.7
QY19-10-3	3.8	18.3	0.8	8.1	2.8	193	52	0.72	17.3	0.5	24.2	0.6

QY19-10-4	3.1	17.6	0.8	7.3	2.9	264	47	0.68	19.8	0.9	29.0	1.3
QY19-10-5	2.3	11.6	0.5	5.0	2.4	166	44	0.67	19.7	0.6	29.3	0.9
QY19-10-6	2.0	10.6	0.5	4.5	4.6	204	56	0.73	20.3	0.5	27.7	0.7
QY19-10-7	1.5	6.5	0.3	3.0	2.4	158	45	0.68	20.2	0.6	29.7	0.8
<b>QY19-10</b>											<b>27.9</b>	<b>1.7</b>
QY19-11-1	5.2	13.4	1.0	8.4	10.7	341	73	0.81	21.6	0.5	26.6	0.6
QY19-11-2	10.0	12.4	1.3	12.9	6.4	283	66	0.78	18.7	0.5	23.9	0.7
QY19-11-3	5.3	13.9	0.8	8.5	8.2	270	70	0.81	18.0	0.4	22.2	0.5
QY19-11-4	2.9	7.8	0.5	4.7	15.1	271	85	0.82	20.4	0.4	24.8	0.4
QY19-11-5	2.0	7.2	0.4	3.7	16.8	343	83	0.82	20.9	0.3	25.5	0.4
QY19-11-6	2.2	7.9	0.4	4.0	14.1	258	84	0.82	18.5	0.4	22.5	0.4
<b>QY19-11</b>											<b>24.2</b>	<b>1.6</b>
<b>Xingtai Transect</b>												
XT19-1-1	18.6	100.5	6.1	42.2	1.8	142	48	0.69	26.5	0.6	38.5	0.8
XT19-1-2	22.1	138.2	7.7	54.5	1.9	198	43	0.66	25.9	0.9	39.6	1.4
XT19-1-3	17.5	47.8	4.2	28.7	1.4	152	42	0.66	27.1	0.7	41.2	1.1
XT19-1-4	2.9	82.8	2.9	22.3	6.6	205	65	0.76	24.1	0.4	31.8	0.6
XT19-1-5	11.3	86.5	5.4	31.6	5.0	194	58	0.74	31.2	0.5	42.0	0.7
<b>XT19-1</b>											<b>38.6</b>	<b>3.6</b>
XT19-2-1	5.1	97.3	3.4	27.9	3.8	200	59	0.74	22.3	0.4	30.1	0.6
XT19-2-2	8.8	53.0	3.1	21.2	4.6	178	57	0.74	26.8	0.5	36.2	0.7
XT19-2-3	4.8	18.2	1.3	9.1	5.5	198	60	0.76	27.1	0.5	35.9	0.6
XT19-2-4	10.0	54.4	2.1	22.8	5.0	149	61	0.75	16.9	0.3	22.4	0.4
XT19-2-5	12.6	77.9	2.8	30.9	3.8	158	55	0.73	16.8	0.3	23.1	0.4
<b>XT19-2</b>											<b>29.5</b>	<b>6.0</b>
XT19-3-1	3.9	865.2	20.4	206.8	3.5	257	52	0.69	18.1	0.7	26.1	1.0
XT19-3-2	1.8	941.4	24.5	222.5	3.4	242	52	0.70	20.2	0.8	29.0	1.1
XT19-3-3	1.7	596.0	15.0	141.5	2.6	213	49	0.68	19.4	0.3	28.6	0.5
XT19-3-4	1.7	485.9	11.4	115.7	4.4	209	54	0.71	18.1	0.3	25.3	0.5
XT19-3-5	1.0	378.8	7.9	89.8	3.9	198	52	0.70	16.1	0.3	23.0	0.4
XT19-3-6	1.1	398.0	10.5	94.4	4.9	209	57	0.73	20.4	0.4	28.2	0.5
XT19-3-7	0.9	345.1	8.1	81.8	7.4	233	66	0.76	18.2	0.4	23.9	0.5

XT19-3-8	1.4	395.8	9.2	94.2	6.8	231	63	0.75	18.0	0.3	23.9	0.4
XT19-3-9	1.4	597.2	14.8	141.4	3.9	206	52	0.70	19.1	0.3	27.3	0.5
<b>XT19-3</b>											<b>26.1</b>	<b>2.1</b>
XT19-5-1	16.0	1.2	4.7	16.3	12.1	230	80	0.82	52.6	1.1	63.8	1.3
XT19-5-2	18.4	0.9	5.1	18.6	13.5	291	80	0.82	50.3	1.1	61.2	1.3
XT19-5-3	11.6	1.1	3.1	11.9	11.6	266	77	0.81	48.0	1.1	58.9	1.3
XT19-5-4	17.9	1.3	4.7	18.2	11.5	228	79	0.82	47.0	1.0	57.3	1.2
XT19-5-5	18.1	0.9	4.9	18.3	19.7	299	93	0.85	49.5	1.0	58.5	1.2
<b>XT19-5<sup>#</sup></b>											<b>59.9</b>	<b>2.3</b>
XT19-6-1	51.2	12.0	10.8	54.0	18.4	371	90	0.86	36.8	0.7	42.9	0.8
XT19-6-2	33.2	11.7	7.6	35.9	7.0	278	69	0.80	39.3	0.8	49.3	1.0
XT19-6-3	23.3	10.6	5.7	25.8	22.3	344	94	0.85	40.9	0.8	48.1	0.9
XT19-6-4	30.7	2.7	6.2	31.4	11.1	323	71	0.81	36.6	0.8	45.3	1.0
XT19-6-5	20.0	7.4	4.7	21.7	36.6	491	120	0.88	40.4	0.7	45.8	0.8
<b>XT19-6<sup>#</sup></b>											<b>46.3</b>	<b>2.2</b>
XT19-7-1	9.5	1.1	1.3	9.8	6.9	237	67	0.80	24.5	0.6	30.6	0.8
XT19-7-2**	14.4	1.6	3.4	14.7	6.3	205	63	0.78	41.9	0.9	53.8	1.2
XT19-7-3**	5.2	0.4	1.2	5.3	30.1	284	110	0.87	42.1	1.0	48.4	1.2
<b>XT19-7</b>											<b>30.6</b>	<b>0.8</b>
XT19-8-1**	2.5	1.6	0.5	2.9	12.5	266	79	0.82	33.6	0.9	40.8	1.1
XT19-8-2	2.8	1.8	0.4	3.2	13.5	329	88	0.84	21.5	0.7	25.6	0.9
XT19-8-3**	3.1	2.5	0.7	3.7	10.0	295	80	0.82	32.4	0.9	39.3	1.0
XT19-8-4**	2.9	2.6	0.6	3.5	6.1	249	68	0.79	32.2	1.5	40.7	1.9
XT19-8-5**	3.7	1.3	0.7	4.0	26.9	268	106	0.86	32.0	0.7	37.0	0.8
<b>XT19-8</b>											<b>25.6</b>	<b>0.9</b>
XT19-9-1	8.4	10.5	2.3	10.8	21.7	280	98	0.85	39.3	0.7	46.3	0.9
XT19-9-2	13.9	47.7	5.7	25.1	27.1	275	106	0.86	41.8	1.1	48.7	1.3
<b>XT19-9<sup>#</sup></b>											<b>47.5</b>	<b>1.2</b>
XT19-10-1	99.3	40.5	23.1	108.8	6.5	210	64	0.78	39.0	0.8	50.1	1.0
XT19-10-2	84.8	27.9	22.0	91.3	10.0	226	75	0.81	44.3	0.9	54.7	1.1
XT19-10-3	197.7	72.9	50.5	214.8	9.6	212	74	0.81	43.2	0.8	53.4	1.0
XT19-10-4	157.6	35.3	42.7	165.8	16.3	297	86	0.83	47.3	0.9	56.8	1.1



XT19-10-5	107.0	17.4	23.0	111.1	9.8	198	76	0.81	38.0	0.7	46.8	0.9
<b>XT19-10<sup>#</sup></b>											<b>52.4</b>	<b>3.5</b>
XT19-12-1	0.9	8.6	0.4	2.9	9.9	220	75	0.79	26.8	0.5	33.7	0.7
XT19-12-2	0.8	5.0	0.3	1.9	9.3	209	74	0.79	24.5	0.6	30.9	0.8
XT19-12-3	1.7	9.2	0.3	3.9	3.8	158	55	0.73	15.4	0.6	21.2	0.8
XT19-12-4	1.8	16.9	0.6	5.8	4.1	152	57	0.73	18.3	0.3	24.9	0.5
XT19-12-5	1.1	9.4	0.3	3.3	6.0	183	64	0.76	17.0	0.4	22.2	0.5
<b>XT19-12</b>											<b>26.6</b>	<b>4.9</b>

---

\*Ft is alpha-correction after ref.XX (Farly, 1996).

##Uncertainties of the mean ages are reported as an average standard deviation for each sample.

\*\*Anomalously old age excluded from calculation of mean age and standard deviation.

#Anomalously old mean Ahe age excluded from interpretation on cooling/exhumation history and thermal history modeling.

**Table S3 Apatite fission track data from the Quyang and Xingtai transects**

Sample	Nc	ps ( $\times 10^5 \text{ cm}^{-2}$ ) (Ns)	U (ppm)	P( $\chi^2$ ) %	ML $\pm 1\sigma$ ( $\mu\text{m}$ ) (Nj)	Standard deviation	D <sub>par</sub> ( $\mu\text{m}$ )	Age (Ma)	err ( $1\sigma$ )
<b><i>Quyang transect</i></b>									
QY19-1	28	5.57 (1165)	14.89	40	12.58 $\pm$ 0.20 (51)	1.46	1.77	76.4	2.6
QY19-2	31	3.15 (880)	14.17	14	13.29 $\pm$ 0.27 (31)	1.48	1.65	49.6	2.1
QY19-3	23	1.18 (313)	5.03	63	12.80 $\pm$ 0.30 (49)	2.15	1.79	47.1	3.1
QY19-4	24	1.78 (283)	7.31	21	12.90 $\pm$ 0.76 (5)	1.69	1.74	59.9	4.4
QY19-5	30	2.37 (850)	11.42	23	12.91 $\pm$ 0.17 (103)	1.77	1.81	40.7	1.6
QY19-6	32	0.95 (328)	2.11	98	13.65 $\pm$ 0.48 (6)	1.17	1.81	89.0	4.9
QY19-7	25	0.85 (188)	2.18	100	12.23 $\pm$ 1.20 (3)	2.07	2.06	76.0	5.6
QY19-8	31	0.91 (222)	2.11	94	13.33 $\pm$ 0.55 (11)	1.82	2.00	87.1	5.9
QY19-9	33	0.86 (256)	2.46	92	14.13 $\pm$ 0.44 (16)	1.74	2.19	69.9	4.4
QY19-10	24	0.9 (121)	3.36	100	13.43 $\pm$ 0.50 (12)	1.72	2.27	56.6	5.2
QY19-11	33	0.80 (258)	3.42	94	12.49 $\pm$ 0.48 (19)	2.08	1.84	46.8	2.9
<b><i>Xingtai transect</i></b>									
XT19-1	29	5.07 (955)	24.16	99	13.15 $\pm$ 0.19 (71)	1.63	1.79	44.4	1.6
XT19-2	27	4.00 (1168)	23.32	45	13.10 $\pm$ 0.14 (112)	1.44	1.75	41.3	1.4
XT19-3	25	4.19 (396)	24.62	99	13.39 $\pm$ 0.20 (43)	1.29	1.71	32.6	1.7
XT19-5	23	4.30 (392)	21.33	93	12.89 $\pm$ 0.34 (14)	1.27	1.91	34.2	1.8
XT19-6	23	5.55 (1377)	37.35	75	13.24 $\pm$ 0.12 (115)	1.26	1.73	28.4	0.8
XT19-7	23	1.36 (200)	8.30	100	12.94 $\pm$ 0.50 (15)	2.02	1.63	33.9	2.4
XT19-9	22	3.45 (852)	25.81	89	13.28 $\pm$ 0.14 (106)	1.44	1.60	25.9	0.9
XT19-10	24	14.4 (1641)	101.79	40	13.20 $\pm$ 0.12 (151)	1.47	1.83	28.2	0.8

Note: Nc, number of dated apatite crystals per sample; ps, spontaneous track density; Ns, number of fission tracks counted; U, uranium concentration measured using LA-ICP-MS; P( $\chi^2$ ), chi-squared probability for (n-1) degrees of freedom; ML, mean confined fission track length; Nj, number of confined fission-track lengths measured; D<sub>par</sub>, arithmetic mean fission-track etch figure diameter parallel to the crystallographic c-axis; Age, reported as central ages calculated using Radial Plotter program with  $1\sigma$  error.